Final Draft
of the original manuscript:

Horstmann, J.; Falchetti, S.; Wackermann, C.; Maresca, S.; Caruso, M.J.;
Graber, H.C.:

**Tropical Cyclone Winds Retrieved From C-Band Cross-Polarized
Synthetic Aperture Radar**

High Resolution Tropical Cyclone Winds Retrieved from Satellite Borne C-band Cross Polarized Synthetic Aperture Radar

Jochen Horstmann[1,2], Silvia Falchetti[2], Christopher Wackerman[3], Salvatore Maresca[2], Michael Caruso[4], and Hans C. Graber[4]

[1]Helmholtz-Zentrum Geesthacht, Geesthacht, Germany
[2]Center for Maritime Research and Experimentation, La Spezia, Italy
[3]General Dynamics Advanced Information Systems, Ypsilanti, USA
[4]Center for Southeastern Tropical Advanced Remote Sensing, Miami, USA

Abstract: This paper presents a geophysical model function (GMF) that has been developed to describe the relation of the ocean surface wind with the normalized radar cross section (NRCS) at C-band cross polarization. Synthetic aperture radar (SAR) images have been collected simultaneously at co-polarization (co-pol) and cross polarization (cross-pol) at moderate to high wind speeds. Using the SAR co-pol retrieved wind fields as well as an uncertainty estimate of the retrieved wind speeds, the cross-pol dependencies of the NRCS are investigated with respect to wind, incidence angle and polarization pairs. For wind speeds above 10 m/s there is a significant dependence of the NRCS on wind speed. However, the SAR cross-pol data are also significantly affected by the noise floor and cross talk between the channels. Estimates of the noise floor are determined and removed from the NRCS. These observations resulted in the development of three GMFs: the first is for transmission at horizontal (H) polarization and the second at vertical (V) polarization. A third GMF accounts for wind direction dependence. A fourth GMF accounting for the wind direction dependence for V polarization could not be estimated due to the lack of SAR data. Validation of the GMFs is conducted by comparison to collocated Stepped Frequency Microwave Radiometer (SFMR) data. The resulting bias of -0.7 m/s and standard deviation of 3.7 m/s demonstrates the excellent performance for these GMFs for wind speed retrieval between 10 and 35 m/s. Furthermore, comparisons show that SAR cross-pol retrieved wind speeds are of similar quality as those of SFMR and are significantly better in the moderate to high wind speed regime than SAR co-pol retrieved winds.

1. Introduction

Tropical cyclones (TC) in the open ocean produce extremely powerful winds, high sea states and torrential rain, which disrupt international shipping. When approaching coasts or making landfall they often generate storm surges and are responsible for extreme destructions and loss of lives. The observation of TC parameters is of major importance for improving their forecast, in particular with regards to strength and propagation. Satellite remote sensing techniques provide a safe and cost effective observation capability for measuring TC parameters. Satellite borne microwave sensors such as scatterometers (SCAT), radiometers and altimeters are particularly useful for this task. They are not dependent on daylight and are capable of penetrating the extreme cloud coverage associated with TC (Katsaros et al., 2002). In the last decade the satellite borne synthetic aperture radar (SAR) imagery has produced substantial interest due to the very high resolution (< 100 m) and large spatial coverage ($\approx$ 500 km) available. SAR images of TC have shown exceptional details on the structure of the storms as well as the potential for estimating various storm parameters (Katsaros et al., 2000). Extensive SAR data of TC have been collected and investigated to improve ocean surface wind field retrieval estimates at moderate to high wind speeds.

Horstmann et al. (2005) showed the capabilities and limitations of measuring quantitative hurricane force surface winds from C-band SAR images using SAR wind retrieval methods,

which are based on the well validated geophysical model function (GMF) CMOD5 (Hersbach et al. 2007). This GMF describes the dependence of the normalized radar cross section (NRCS) on the wind and imaging geometry and is limited by a decreasing sensitivity of the backscatter with increasing wind speed (Shen et al., 2009). Reppuci et al. (2010) addressed this sensitivity by estimating the storm intensities using SAR retrieved wind fields merged with simple numerical TC models. All these investigations were performed with co-pol data acquired either at vertical (V) or horizontal (H) polarization in transmit and receive. Recent studies using cross-pol SAR images (Hwang et al., 2010; Vachon and Wolfe, 2011; Zhang et al., 2011) suggest that the relationship between wind speed and NRCS is independent from incidence angle and wind direction and that there is no saturation effect at high wind speeds. This overcomes the previously mentioned limitations of co-pol SAR data with respect to TC winds (Zhang and Perrie, 2012). Recently, an in depth comparison of SAR co-pol to SAR cross-pol wind speeds under TC conditions was undertaken utilizing the cross-pol GMF developed in this paper. The comparison shows the significantly better performance of SAR cross pol wind speed retrieval in particular at wind speeds above 20 m/s (Horstmann et al., 2013).

Within this study an in depth analysis of the cross-pol NRCS characteristics with respect to wind speeds, wind directions, incidence angles and sensor performance is undertaken utilizing six SAR images acquired under TC conditions. The SAR data were carefully corrected for scalloping (Romeiser et al. 2012), noise floor and beam seams. Using the wind fields retrieved from the co-pol SAR data as well as additional available measurements, a set of new GMF's for cross-pol are developed, which give the dependence of the NRCS on wind speed and wind direction. The GMF's are validated by comparison to collocated wind speed measurements from the Stepped Frequency Microwave Radiometer (SFMR).

In general the ability to measure ocean surface winds from space borne microwave radars operating with co-pol is due to the fact that the local wind field generates small-scale surface roughness that increases with wind speed. For radar backscatter at moderate incident angles (20° to 60°), the NRCS is proportional to the spectral density of the surface roughness on scales comparable to the radar wavelength. In the case of cross-pol the backscatter of the ocean surface is significantly weaker and considered to be primarily caused by ocean surface wave breaking, which in turn is primarily caused by the wind. However, the scattering mechanisms at cross-pol are not as well understood as at co-pol.

The paper is organized as follows. Section 2 introduces all the data available for this investigation. Section 3 describes the correction of the SAR data with respect to scalloping, noise floor and beam seams. In section 4 the wind retrieval from the co-pol SAR data is described, which is used in Section 5 to analyze the dependencies of the cross-pol NRCS and develop the new GMFs. In section 6 the GMFs for cross pol are validated by comparison to the SFMR data. Finally, conclusions and perspectives for future work are presented.

2. Utilized data

This development uses six SAR images collected by the Canadian satellite Radarsat-2 in the ScanSAR wide mode A (SCWA). All images were acquired over TCs and show large parts of the storm system, which provides a large range of wind speeds and directions to investigate the wind dependencies of the NRCS. In the SCWA mode a nominal image scene covers an area of approximately 500 km x 500 km. Multiple scenes may be collected with a resolution of 100 m in azimuth (flight direction) and between 160 m and 72 m from near to far range covering incidence angles between 20° and 49°. The SAR data were acquired at C-band with dual polarization (dual-pol), meaning the satellite was transmitting with either V-pol or H-pol and receiving both polarizations. This results in two images, where one is recorded at co-pol (HH or VV) and another at cross-pol (HV or VH). A significant issue with radars collecting at

multiple polarizations is the antenna isolation performance. If this is too low, the cross-talk affects the NRCS measurements. In case of Radarsat-2 the isolation is better than -32 dB and simulations of Touzi et al. (2010) showed that this will affect mainly NRCS collected at small incidence angles. Radarsat-2 has a very low noise floor in comparison to the other space borne SAR systems in orbit. The noise floor for SCWA data is approximately -28 dB ±2 dB, and is suitable for determining the wind dependence of cross pol NRCS (Hwang et al., 2010; Vachon and Wolfe, 2011; Zhang et al., 2011; Zhang Perrie, 2012).

In addition to the SAR data, several different sources of wind information were available (listed in Table 1), which will be used as 'ground truth' in this analysis. The wind fields from the satellite borne Advanced SCAT (ASCAT) are computed using measurements from the SCAT operating at C-band with vertical polarization in transmit and receive onboard the European organization for the exploitation of Meteorological Satellites (EUMETSAT) Metop-A satellite. The resulting wind fields represent a 10 minute mean neutral wind at a height of 10 m above the surface. ASCAT wind fields cover a 550 km wide swath 350 km shifted to the right and the left of the satellite track. The wind fields are retrieved at either 25 km or 12.5 km resolution with an accuracy of 1.3 m/s in wind speed and 16° in wind direction (Verspeek et al., 2010).

The Stepped Frequency Microwave Radiometer (SFMR) was developed to measure hurricane force ocean surface winds. The instrument is mounted on an aircraft and measures the nadir brightness temperature at four selectable frequencies between 4.5 and 7.2 GHz, which are converted to 1 minute sustained surface wind speed via a GMF. The obtained wind speed measurements have an accuracy of approximately 4 m/s when compared to GPS dropsonde measurements over a range of wind speeds between 10 and 70 m/s (Uhlhorn et al., 2007).

The GPS Dropsonde is an instrument package that is dropped out of an aircraft to record measurements during its descent. As it descends to the surface it measures and transmits the wind speed, wind direction and GPS position along with other information. The GPS Dropsonde also receives GPS navigation signals and measures the Doppler shift of each signal and converts this information to winds at different heights. Only the retrieved 1 minute sustained surface wind are used in this analysis.

Furthermore, wind speed measurements from the WindSat radiometer aboard the Coriolis satellite were available. WindSat operates at five frequencies of which 10.7, 18.7 and 37.0 GHz are fully polarimetric and 6.8 and 23.8 GHz operate only at dual polarization. WindSat wind speeds are utilized as additional information at low to moderate winds but were not considered in the developmeent of the GMF. For details with respect to WindSat refer to Gaiser et al., 2004.

All wind measurements used within this study (Table 1) were corrected for the time differences between SAR acquisition and measurements by shifting the locations of the measured data with respect to the movement of the storm. The movement of the storm is derived from the best track information from the Joint Typhoon Warning Center (JTWC). The storm rotations were not considered during the spatial translation. Figure 1 shows the SAR image of Typhoon Malakas on 22 September 2010 with the original flight track and the adjusted flight track superimposed.

3. Correction of SAR data

The SAR data have to be carefully corrected for image artifacts that are not due to the local surface scattering to eliminate contamination of the retrieved wind. This process includes a correction for scalloping (Romeiser et al. 2012), noise floor and beam seams. Figure 2 depicts a subimage of the SAR acquisition shown in Figure 1 (top image), the subimage after

correction for the noise equivalent sigma naught (middle image), and the subimage after correction for the beams and nadir ambiguity lines (bottom image). Each correction step is discussed below.
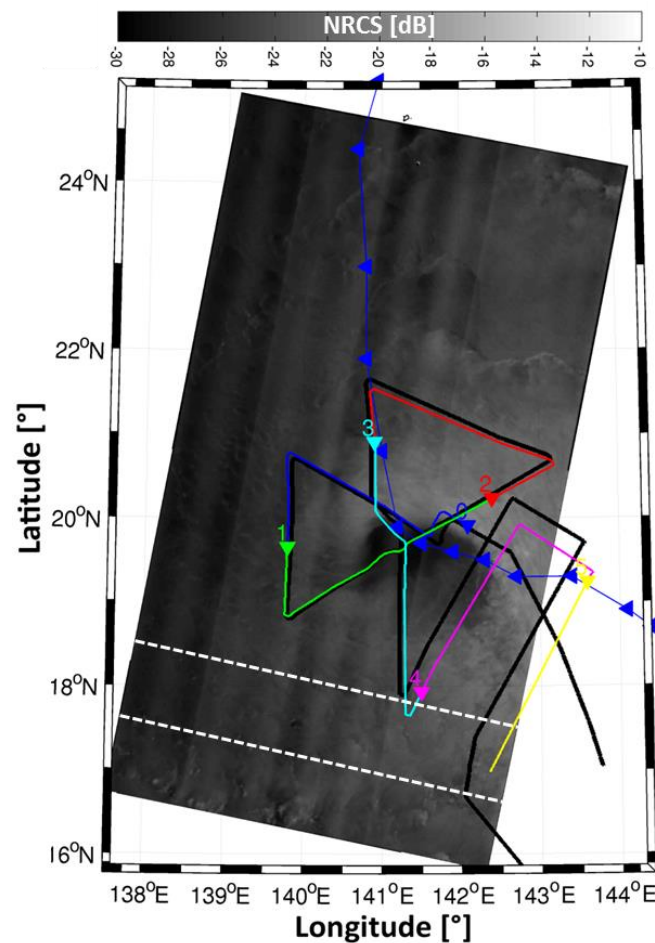

Figure 1: Synthetic aperture radar (SAR) image of Typhoon Malakas acquired by the Canadian satellite Radarsat-2 on the 22 September 2010 at 20:30 UTC at C-band with cross polarization (horizontal in transmit and vertical in receive). Superimposed to the SAR image is the original C-130 flight track (black line) as well as the flight track adjusted for SAR image acquisition time (color coded time line). The blue curve depicts the best track data of the Typhoon where the triangles present a one hour time step. The white dashed lines mark the area which is being used for demonstrating the SAR data correction (Figure 2).

3.1 Scalloping removal

The first step is to correct the scalloping intrinsic to ScanSAR data. Scalloping is a wave like modulation of the NRCS in near-azimuth direction and produces unrealistic artifacts in the SAR wind retrieval. The amount of scalloping present in a ScanSAR image varies substantially from scene to scene. The approach proposed by Romeiser et al. (2012), which identifies the direction, wave length and higher harmonics of the scalloping pattern in the spectral domain was used to remove the scalloping patterns in the Radarsat-2 data. Therefore, energy is subtracted in the image spectra from the detected scalloping peaks and a division is performed in the spatial domain to account for the multiplicative nature of the scalloping pattern. This process is done in an iterative manner and has been shown to remove scalloping

very effectively without pronounced changes of other properties of the image (e.g. mean image spectra or rms variability) affecting the wind retrieval.

3.2 Noise Floor Correction

The second step is to correct the data for the contribution of the noise equivalent sigma naught (hereafter noise floor). This is a measure of the sensitivity of the radar to areas of low backscatter. Features which have a backscatter below this threshold are difficult to distinguish. The noise floor varies within ±2 dB over the range (look direction) of the image, adds to the backscatter of the image and adds incidence dependence to the NRCS (see Figure 3). The contribution of the noise floor must be removed from the measured NRCS to produce a consistent GMF. This correction is particularly important for the data collected at cross polarization as the measured NRCS are very low (typically < -23 dB) and close to the noise floor (-28 dB ±2 dB for the imagery used within this study).
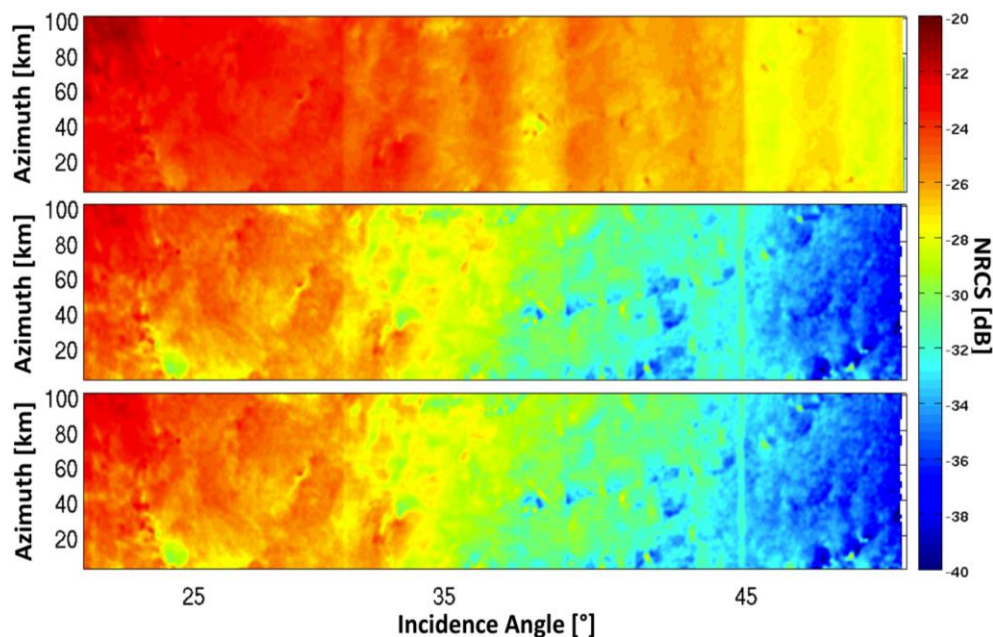

Figure 2: Subimage of the Radarsat-2 ScanSAR image acquired on the 22 September 2010 at 20:30 UTC in cross polarization (pol) showing the different correction steps applied. Depicted are from top to bottom the original image, image corrected for noise equivalent sigma naught, and finally for the beams and nadir ambiguity lines.

The top panel in Figure 2 shows the uncorrected NRCS where the effects of the noise floor are visible as undulating patterns of brighter and darker areas across the range. After subtracting the noise floor contribution from the NRCS, the majority of these features have disappeared (Figure 2 center panel). In Figure 3 the incidence angle dependence (range) of the NRCS is shown before and after the noise floor correction was applied. In these plots the NRCS was integrated over 100 km along the azimuth direction (the vertical axes shown in Figure 2). The noise floor is provided within the ScanSAR data and was estimated by a model that accounts for the characteristics of the payload, beam mode, acquisition, and the ground processing. The estimate is expected to be known to better than 1 dB (MDA, 2011). Due to the much higher backscatter in co-pol SAR images the noise floor contribution is minor and can be neglected for wind speed retrieval purposes at moderate to high winds. In case of SAR cross-pol data the contribution is major and can make a difference of over 10 dB.
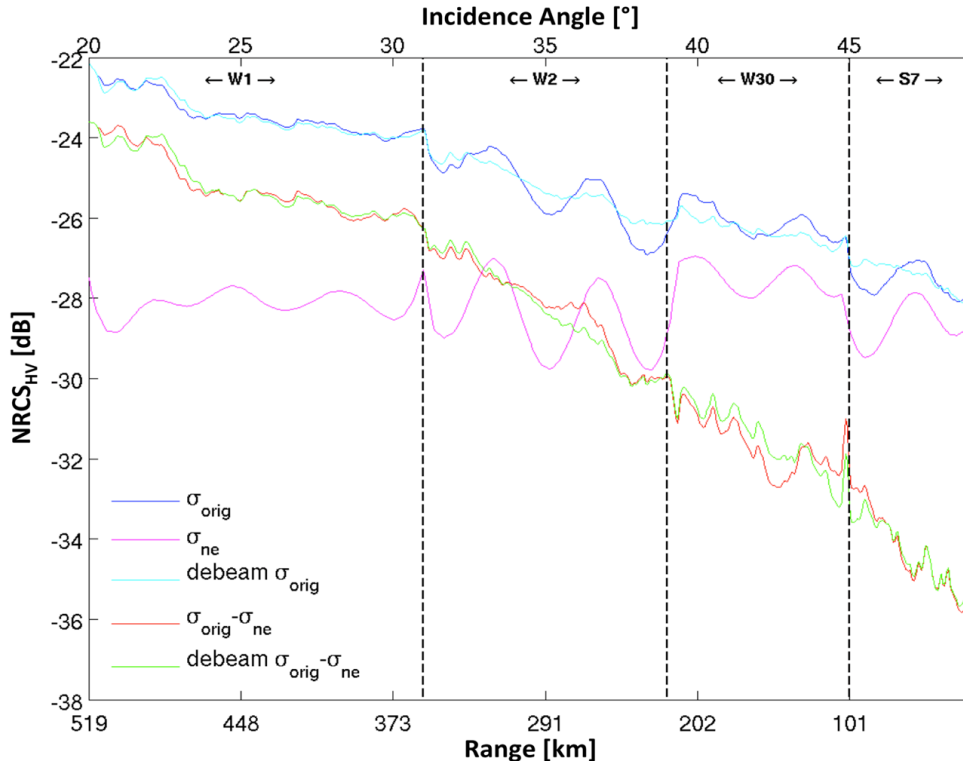
Figure 3: Contribution of the noise floor to the normalized radar cross section (NRCS) of the cross-pol Radarsat-2 ScanSAR image acquired on the 22 September 2010 at 20:30 UTC. The dark blue line represents original NRCS S_{orig}, the pink line the noise equivalent sigma naught (noise floor) S_{ne}, the light blue NRCS corrected for beam seams debeam S_{orig}, the red line NRCS corrected for noise floor $S_{orig} - S_{ne}$, and the green line NRCS corrected for noise floor and beam seams debeam $S_{orig} - S_{ne}$.

3.4 Removal of beams and nadir ambiguities

An additional artifact inherent in ScanSAR images occurs when images are formed in range using different physical radar transmit/receive beams across the different range locations. This results in a series of beams across the SAR swath with slightly different antenna patterns, overall scale factors, and noise floors. This causes an image modulation in range that can be particularly egregious at the edges between beams (i.e. "beam seams"). Spurious wind directions are generated when the wind retrieval algorithm aligns with the beam seam edges instead of wind induced streaks. In addition, the locations of these beam patterns can drift slightly as a function of the azimuth location of the image. To remove these modulations, an automated process has been developed that divides the image into 10 azimuth blocks and generates a scaling function in range for each block to remove the beam patterns. The scaling functions are generate by first averaging the image range lines over each azimuth block (first removing image pixels that are too bright or dark based on the overall image statistics), smoothing in range (using a smoothing filter of 21 pixels), converting from energy to dB, then fitting a fourth order polynomial to the resulting function curve. The scaling functions for each azimuth block are then generated using the ratio of the polynomial fit (converted back to power) to the smoothed range functions. A bi-linear interpolation is performed between scale functions from each azimuth block to provide a smooth correction function over azimuth and range.

Finally, SAR images can often have an ambiguous nadir response, which comes from the double bounce between the satellite and the actual nadir location on the ground. This usually appears in the far range as a bright line in the image, particularly when the nadir response is from the ocean. This is removed from the image at the same time as the beam patterns by examining the derivation in range of the average-smoothed range plot. The ambiguous nadir line will be between two locations with large derivatives and opposite signs. If such derivative pairs are located in the imagery, the values between them are replaced with noisy data whose mean is a linear function that is set by the mean value of the image at either side of the nadir line and whose standard deviation is generated by averaging N independent exponentially-distributed random variables (i.e. N-look speckle noise) where N is derived from the image statistics on either side of the nadir line.

4. SAR wind retrieval using co-polarized data

For ocean surface wind field retrieval from co-pol SAR data the wind directions are retrieved from wind-induced phenomena that are aligned in wind direction (Gerling, 1986; Wackerman et al., 1996; Lehner et al. 1998). The orientations of these features are derived by the Local Gradient (LG) Method (Horstmann et al. 2002, 2005; Koch, 2004). Therefore, the SAR image is sequentially smoothed and reduced to resolutions of 100, 200, and 400 m, resulting in three images. From each of these smoothed images, local directions defined by the normal to the local gradient are computed (with a 180° ambiguity). Pixels associated with land, surface slicks, and strong rain are masked and excluded from the analysis by considering land masks and several parameters retrieved from the SAR image (Koch, 2004). From all the retrieved local directions on the different scales the most frequent directions in a predefined grid cell (here 20 km) are computed. As all images considered in this study were acquired over tropical cyclone (TC) eyes the removal of the directional ambiguities resulting from the various scales were resolved by selecting in each grid cell the direction, which is closest to a circular direction around the center of the TC's eye assuming 15° inflow near the eye and decreasing to a 0° inflow in a distance of 150 km from the TC's eye. For grid cells at a larger distance to the TC's eye the nearest direction to its neighboring grid cell is selected (starting from the center of the TC's eye).

Wind speeds are retrieved from co-pol SAR data utilizing a GMF that provides the NRCS as a function of the equivalent neutral wind vector at 10 m anemometer height, incidence angle, wind direction with respect to the radar look direction, radar frequency, and polarization. For C-band, VV-polarization, there are a number of popular model functions of which the most commonly used is the Cmod5n (Hersbach et al., 2010). Each of these GMFs is directly applicable for wind speed retrieval from C-band VV pol SAR images. For SAR images acquired at HH-polarization, no similar well developed GMF exists. To meet this deficiency a hybrid model function is used that consists of a C-band polarization ratio (PR) and one of the prior mentioned GMFs (Horstmann et al., 2000; Vachon and Dobson, 2000). The optimal PR value is uncertain and a variety of ratios have been proposed (Thompson et al. 1998; Mouche et al., 2005; Zhang et al., 2011). In this analysis, the PR suggested by Thompson et al. (1998) is utilized, which neglects wind-speed and wind direction dependence and is given by

$$PR = \frac{\left(1+\alpha \tan^2 \theta\right)^2}{(1+2\tan^2 \theta)^2} \tag{1}$$

where θ is the incidence angle and α is a constant, which varies in literature between 0.4 and 1.2 (Horstmann et al. 2000; Vachon and Dobson, 2000; Monaldo et al.,2004; Horstmann and Koch, 2005). Within this study we have used an α of 0.8.

Using the above described wind retrieval scheme all of the co-pol SAR data were converted into wind fields. Wind directions were retrieved with a 20 km resolution and extrapolated to

a resolution of 1000 m, which represents the final resolution of the wind speeds. In Figure 4 (left hand side) the wind field resulting from the co-pol SAR image (Figure 1) of Typhoon Malakas is depicted. For comparison, the SFMR wind speeds corrected for the time differences between SAR acquisition and SFMR measurements are shown as circles with the colors representing wind speed using the same scale as the SAR wind field. In general there is a fairly good agreement for wind speeds up to 25 m/s and increasing error with increasing wind speed and decreasing incidence angle (see also Figure 10).
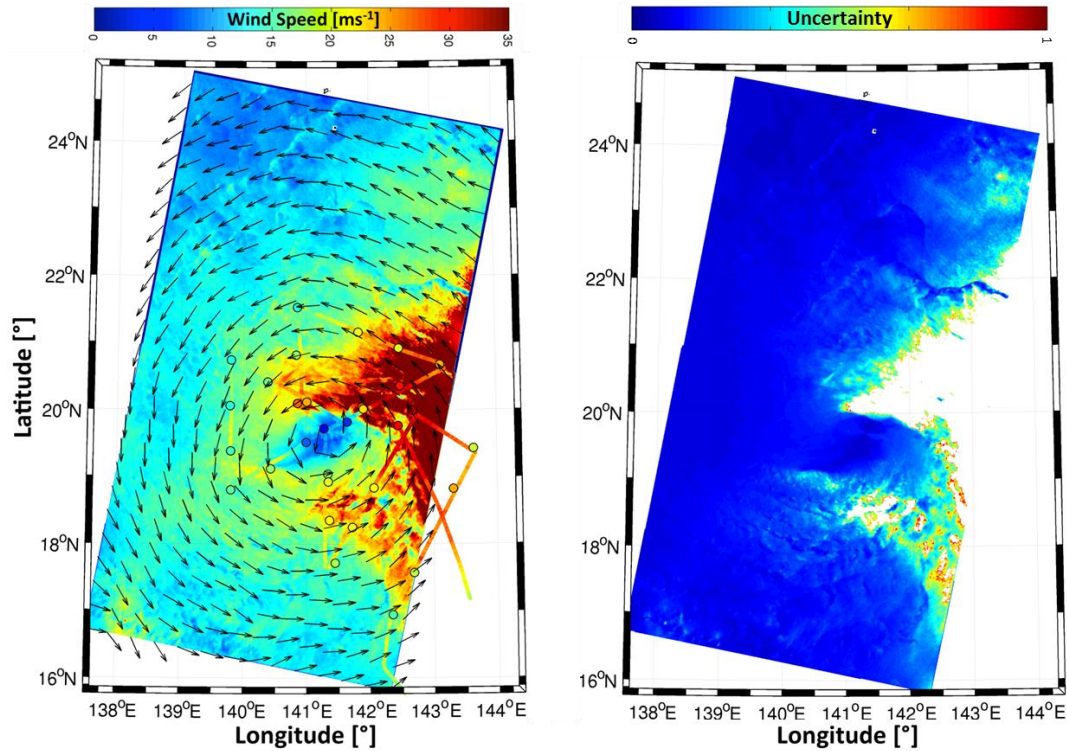

Figure 4: The left hand side shows the wind field of Typhoon Malakas retrieved from the Radarsat-2 ScanSAR image acquired at HH pol (Figure 1). The SFMR surface wind speeds shifted to account for the acquisition time difference are shown as the color coded line. The right hand side depicts the SAR retrieved uncertainty mask of the wind speeds.

In addition to the high-resolution wind fields the uncertainty of the SAR retrieved wind speed is estimated. The wind speed at every SAR grid point is computed assuming an uncertainty of the NRCS of ± 0.5 dB. The resulting wind speed uncertainty is plotted in Figure 4 (right hand side) showing high uncertainties at high wind speeds and small incidence angles. The regions masked in white denote areas where the uncertainty estimate cannot be calculated as the NRCS with the added 0.5 dB uncertainty is above the definition range of the GMF. In these areas the uncertainty of the wind speed is particular high due to a very low dependence of NRCS on wind speed. In general the white areas represent the areas with the largest differences in between SFMR and SAR retrieved wind speeds.

5. Geophysical model function for cross polarized SAR data

The dependency of the cross-pol NRCS on wind speed is shown in Figure 5 using the five images collected at HV-pol listed in Table 1. For comparison with Vachon and Wolfe (2011) and Zhang and Perrie (2012), the NRCS was not corrected for the noise floor but for scalloping, beams and nadir ambiguity lines. The wind speeds corresponding to the density plot and the contour lines were retrieved from the Radarsat-2 co-pol SAR data as described in

Section 4. For this plot, all the grid points with an moderate to high uncertainty and those for which the uncertainty can not be calculated (white regions in Figure 4 left hand side) have been excluded. For each of the color-coded symbols, the wind speeds correspond to ASCAT, WindSAT, GPS sonde and SFMR measurements with the respective cross-pol NRCS values. For this purpose the SFMR flight track locations as well as GPS sonde were corrected for the time lag between flight and SAR acquisition (see Section 2). Superimposed on these plots are the empirical GMF's for cross pol wind retrieval suggested by Vachon and Wolfe (2011) and Zhang and Perrie (2012). These GMFs were fitted to Radarsat-2 SAR fine quad-pol data considering co-located buoy wind speed measurements of up to 22.5 m/s.
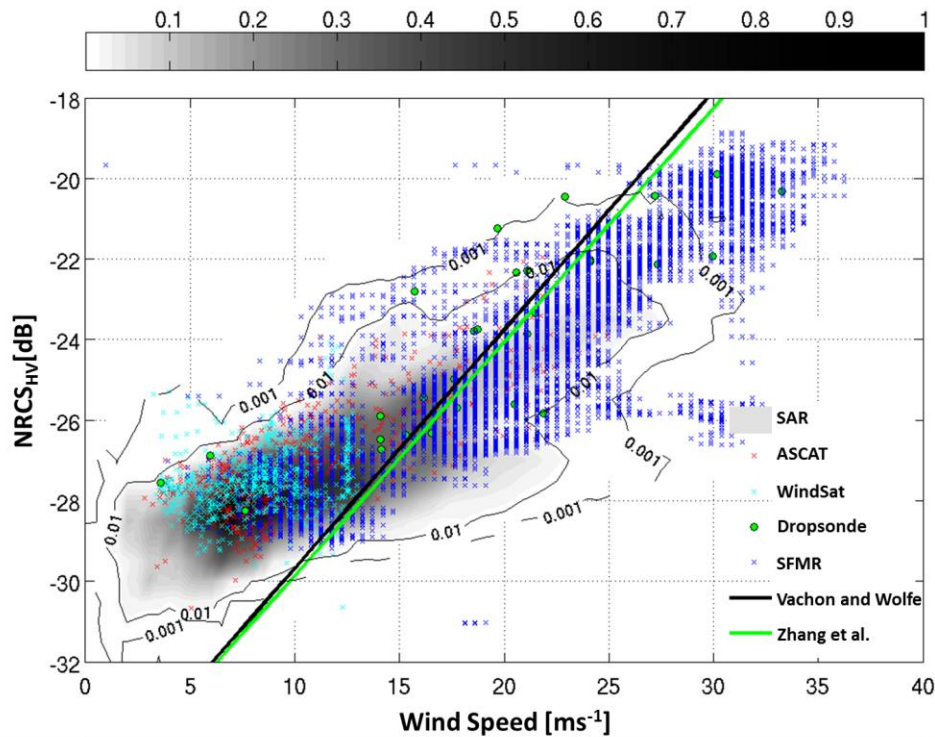

Figure 5: Dependency of the noise floor uncorrected but debeamed cross-pol NRCS on wind speed using all Radarsat-2 ScanSAR scenes (HV-pol) listed in Table 1. The underlying density plot represents the co-pol retrieved wind speed versus cross-pol NRCS. The superimposed symbols represent measurements from different sources as given in the legend. Superimposed is the fit from Vachon and Wolfe, 2011 as well as Zhang et al., 2011. Note that these GMFs should not be applied to data close or below the noise floor (< 27 dB in case of Radarsat-2 ScanSAR data).

Name of storm	Image date and time (GMT)	Saffir-Simpson hurricane scale	Available wind measurements
Earl	Sep 2, 2010 22:59	2	ASCAT; SFMR
Fanapi	Sep 13, 2010 09:09	tropical storm	ASCAT
Fanapi	Sep 17, 2010 21:15	2	SFMR; Dropsonde
Malakas	Sep 22, 2010 20:30	tropical storm	SFMR; Dropsonde
Malakas	Sep 24, 2010 08:45	2	ASCAT; WindSat
Megi	Oct 14, 2010 09:02	tropical storm	ASCAT; SFMR; WindSat

Table 1: Available Radarsat-2 SAR data with collocated 'ground truth' measurements from the airborne Stepped Frequency Microwave Radiometer (SFMR), Dropsondes, the satellite borne Advanced Scatterometer (ASCAT) and the WindSat Radiometer (WindSat).

It can be seen that the Radarsat-2 quad-pol retrieved GMF does not reflect the dependence shown by the Radarsat-2 SAR SCWA data. In the low to moderate wind speed range, this is most likely due to the significantly higher noise floor of SCWA data (-28 dB ±2 dB) in comparison to the fine quad-pol data (-36.5 dB ±3 dB) used for the GMF's shown in Figure 5. An additional contribution could be from the cross talk between the antennae channels. This is about -32 dB for SAR SCWA data, while the quad-pol data has been corrected by up to -45 dB (Vachon and Wolfe, 2011).
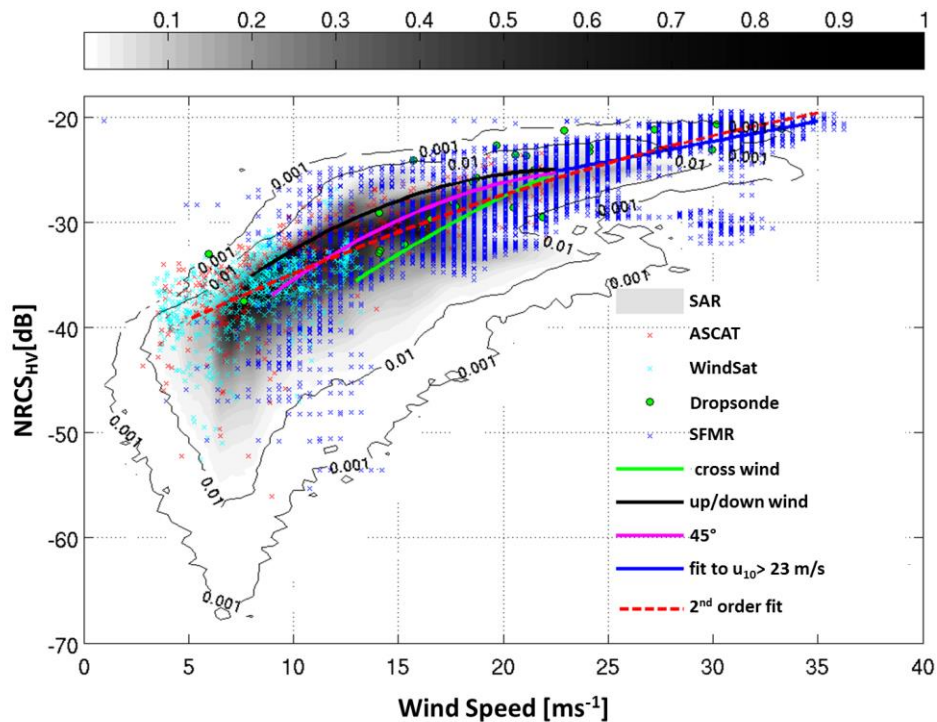

Figure 6: The same plot as in Figure 5 but considering noise floor corrected cross pol NRCS. Superimposed is the best fit considering no wind directions as well as considering a wind direction dependent GMF.

Figure 6 is the same as Figure 5, except that the noise floor corrected cross pol NRCS data were used. Both the SAR retrieved wind speeds and reference wind speeds show a nonlinear dependence of the NRCS on wind speed as well as an increasing spread with decreasing wind speeds. As expected, the noise floor correction affects the lower backscatter values more than the higher values. For NRCS values near the noise floor, the uncertainty of the noise floor will add significantly to the error in the NRCS. The different color-coded lines represent the GMFs, which will be explained below.

To determine the dependence of the NRCS with respect to incidence angle and wind direction, the NRCS was investigated for wind speeds at 10, 15, and 20 m/s bounded by a ±1 m/s wind speed interval (top to bottom rows in Figure 7). Since we do not have enough spatial coverage of wind speed results from the reference data to derive dependences we utilized the wind speeds derived from the co-pol C-band SAR imagery using the methodology described above. Thus the dependencies were derived by comparing cross-pol NRCS values with the corresponding co-pol derived wind speeds. However, we note that we also show that the reference wind speeds are consistent with these results. The first column in Figure 7 shows the dependence of the NRCS on the wind direction. The wind direction dependence is evident with local backscatter maxima at the up and downwind directions and local minima at the cross wind directions. This dependency decreases with increasing wind speeds. This behavior is unexpected as the investigations of the Radarsat-2 quad-pol data did not

demonstrate a wind direction dependence (Hwang et al., 2010; Vachon and Wolfe, 2011; Zhang et al., 2011). The cross-pol wind direction dependencies observed in Figure 7 are very similar to the well-known dependencies at co-pol. An attempt to model this dependency is given in Section 7. The second and third columns of Figure 7 show the dependence of the NRCS on incidence angle. The data were again subdivided into ±1 m/s wind speed intervals at 10, 15 and 20 m/s and bounded by ±10° cross wind directions (second column) and up-down-wind directions (third column) to remove the previously discussed wind direction dependencies. Although the data available do not cover the entire range of incidence angles and wind speeds, they do not show significant incidence angle dependence. However, recent results of van Zadelhoff et al. (2014) show slightly decreasing cross-pol NRCS with incidence angle, similar to what can be seen in Figure 7 left hand side.
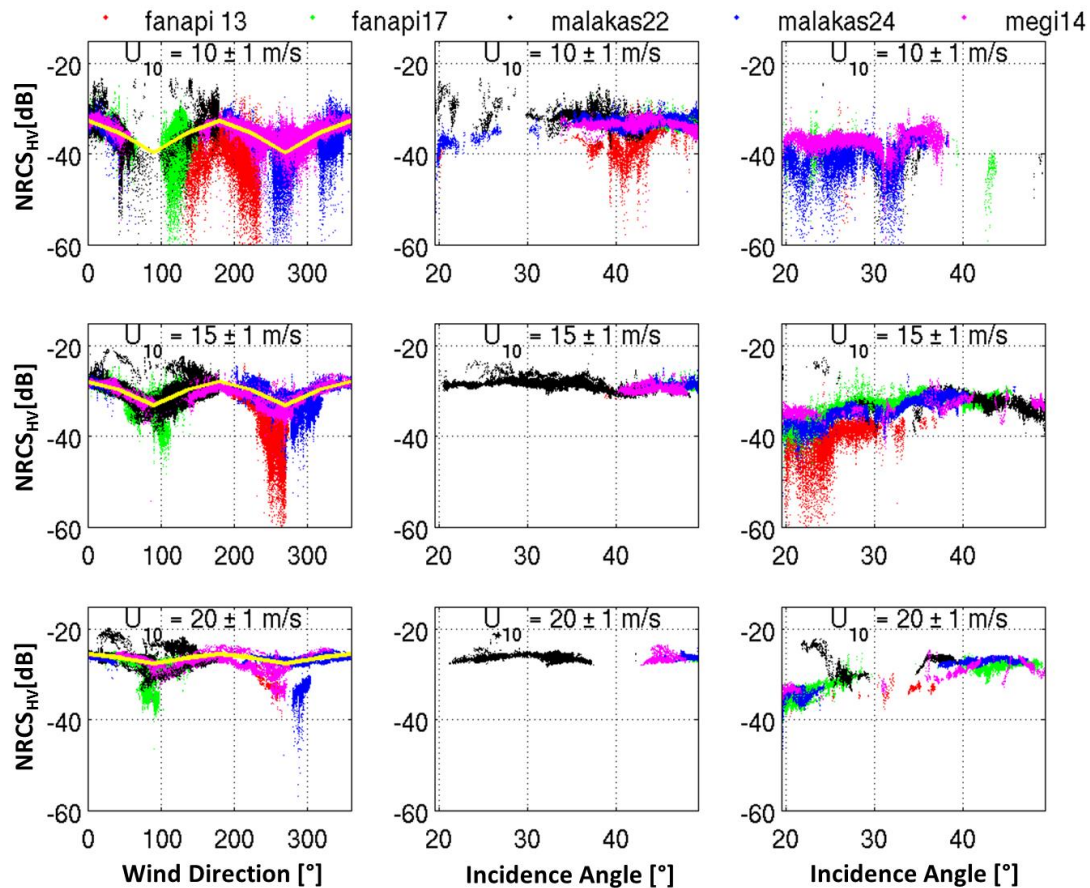

Figure 7: Dependencies of the NRCS on wind directions (first column) and incidence angles for wind directions within ±10° of up- and down-wind directions (second column) and cross wind directions (third column). The different rows from top to bottom represent wind speed intervals of ±1 m/s at 10, 15 and 20 m/s. The yellow line (first column) represents the wind direction dependent GMF.

Therefore, for development of the empirical GMF for cross-pol, only the wind speed and direction were considered. Due to the limited amount of data available and the general dependencies of the NRCS on wind direction observed in the data, no discrimination was made between up- and down-wind, reducing the wind direction dependence to an interval of 90°.

The resulting GMFs are plotted in Figure 6. The red dashed line represents the wind speed dependent only GMF resulting from a second order polynomial fit to the data. The other lines represent the GMFs with an additional wind direction dependency and are plotted for up-

down- wind (black line), cross wind (pink line) and 45° to cross winds (green line). These polynomials were fitted only considering wind speeds below 22.5 m/s. For wind speeds above 22.5 m/s the wind direction dependent GMF loses its wind direction dependency and results in a linear fit (blue line). For this linear fit only wind speeds resulting from SFMR wind speeds were considered, because the error from co-pol retrieved wind speeds increases significantly for high wind speeds. The cross pol GMFs for retrieval of a wind speed are given by:

$$u = a_2 \sigma_0^2 + a_1 \sigma_0 + a_0, \qquad\qquad\qquad\qquad (2)$$

where σ_0 is the cross pol NRCS corrected for the noise floor. In case the wind direction is considered in addition a GMF for up- down wind, diagonal wind as well as cross wind is given. The polynomial coefficients for the GMFs are given in Table 2.

GMF	a_2	a_1	a_0
HV GMF	-0.0089	1.0108	-44.1216
VH GMF	-0.0097	0.7844	-35.8912
HV GMF up/down wind	-0.0429	2.0063	-48.4172
HV GMF diagonal wind	-0.0425	2.1966	-53.2148
HV GMF cross wind	-0.0235	1.9157	-56.5182

Table 2: List of polynomial coefficients for the wind direction independent GMV for HV pol and VH pol as well as the wind direction dependent GMF for HV pol.
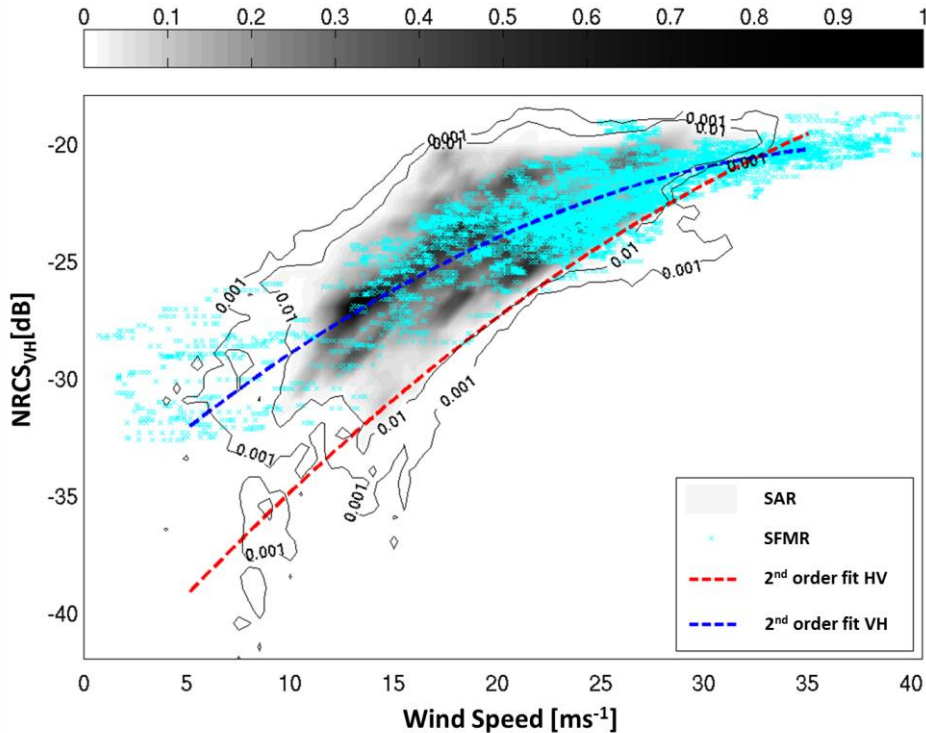

Figure 8: The same plot as in Figure 6 but considering the wind speeds and VH NRCS resulting from the Radarsat-2 ScanSAR image of hurricane Earl. Superimposed are the wind direction independent best fits for HV and VH ScanSAR data.

In Figure 8. the wind speed is plotted versus the corrected cross-pol NRCS resulting from the Radarsat-2 ScanSAR image of hurricane Earl, which was, in contrast to all other investigated cases, acquired at VH pol on 2 September 2010 at 22:59 UTC. As in Figure 6 the density plot represents the co-pol retrieved wind speeds with the corresponding cross-pol NRCS and the symbols represent the SFMR wind speeds at the corresponding cross-pol NRCS. For reasons

we cannot explain at this point the HV pol GMF developed does not represent the situation observed at VH pol so that a extra VH pols GMF had to be elaborated. The resulting wind direction independent GMF's for HV pol and VH pol (Table 2) are superimposed to Figure 8.

6. Validation of GMF

To validate the developed GMFs, the cross-pol retrieved wind speeds were compared to the SFMR surface wind speeds, which were corrected for the acquisition time difference by adjusting the locations with respect to the storms eye. In Figure 9, the SAR cross-pol retrieved wind speeds are plotted for Typhoon Malakas using the wind direction dependent HV GMF. The wind speeds from SFMR are superimposed on the SAR wind map and show that the wind speeds generally agree very well.
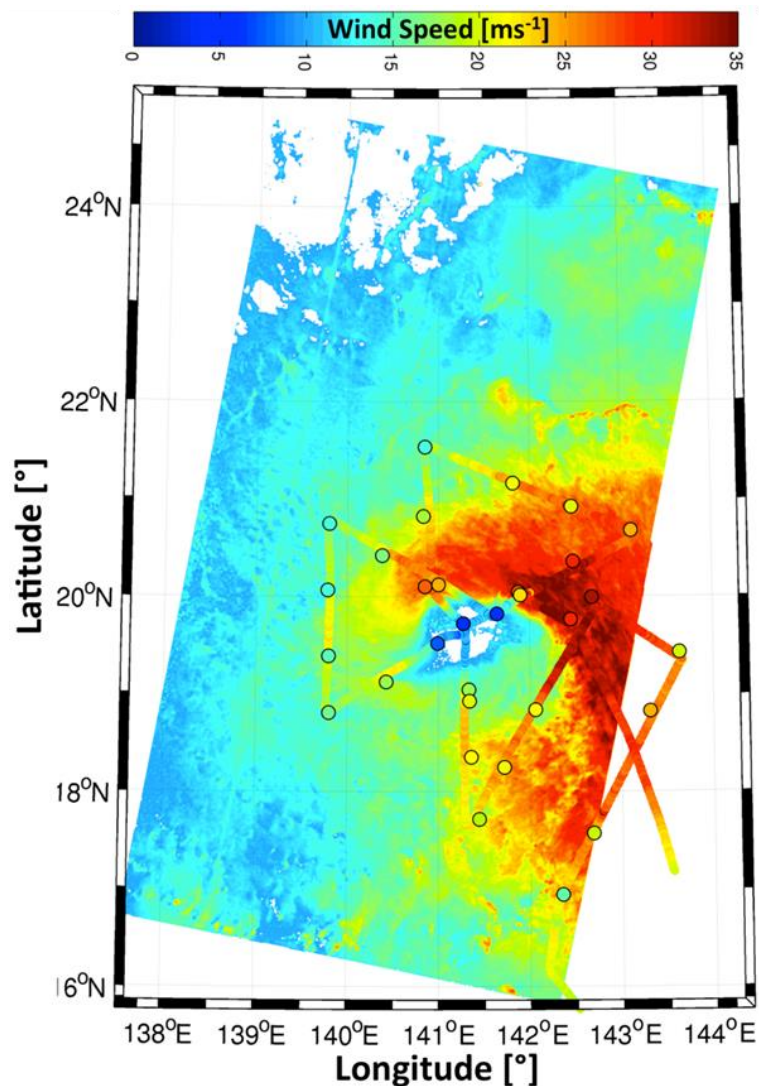

Figure 9: SAR cross pol retrieved wind field of Typhoon Malakas acquired by Radarsat-2 ScanSAR. Superimposed to the SAR wind speeds are the SFMR wind speeds were the flight track was adjusted for SAR image acquisition time.

Figure 10 shows the direct comparison of SFMR to SAR co-pol and cross-pol retrieved wind speeds. In Figure 10 the SAR wind speeds are from the mean NRCS retrieved from the 2 km x 2 km area at the colocation of the SFMR measurement. It can be seen that the cross-pol retrieved wind speeds agree significantly better to SFMR than the co-pol. The biggest

difference between the SAR and SFMR measurements is seen approximately 4.5 h after the SAR acquisition. This is close to the asymmetric eye wall and is very likely due to the time delay and a possible rotation of the storm. The comparison of SAR cross-pol to SFMR wind speeds for this image results in a bias of -0,7 m/s with a standard deviation of 3.8 m/s.
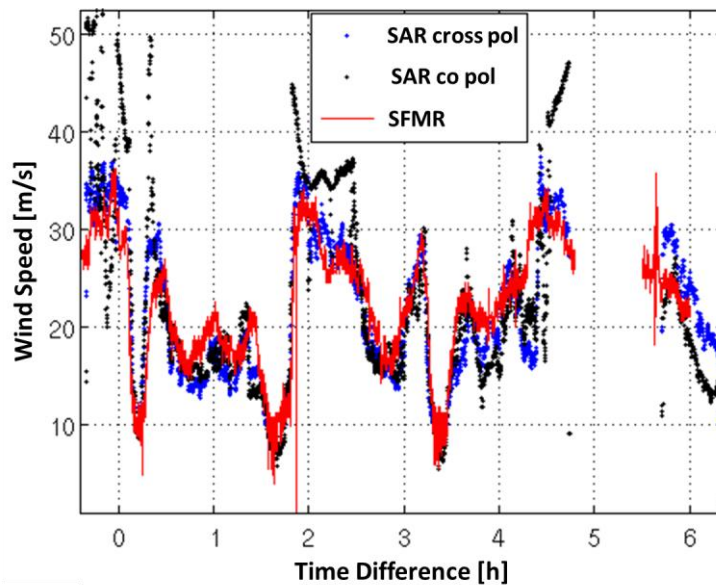

Figure 10: Comparison of SAR cross-pol (blue dots), SAR co-pol (black dots) and SFMR wind speeds along the SFMR flight track.
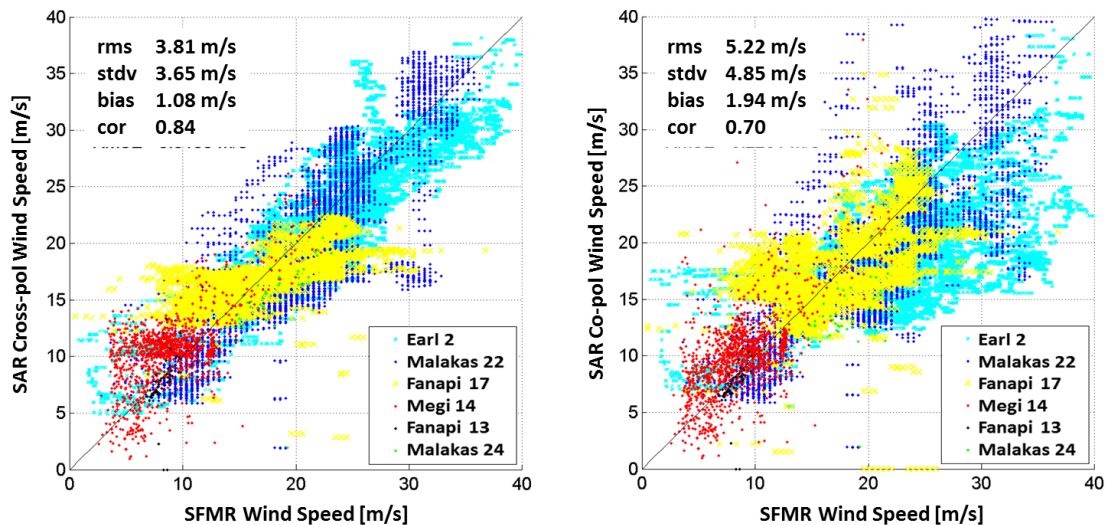

Figure 11: Scatterplot of SAR wind speeds versus SFMR wind speeds considering all SAR data listed in Table 1. Left hand side shows the SAR cross-pol and right hand side the coresponding SAR co-pol results.

Comparison of the SAR cross-pol retrieved wind speeds from all of the cross-pol images available (Table 1) resulted in the scatter plot shown in Figure 11. The wind direction independent GMF for VH pol was used for Hurricane Earl and the wind direction dependent GMF for HV was applied for the other cases. In Table 3 all the statistics are compiled from the different GMFs and polarization pairs. In general wind speed retrieval from cross-pol give significantly better results than from co-pol. At lower wind speeds cross-pol winds suffer from the limitations of the sensor with respect to the noise floor. For wind speeds below

approximately 20 m/s the wind direction dependence becomes more and more significant and better wind speeds are produced using the wind direction dependent GMF for cross-pol. Note that for these results, the wind direction that was used in the GMF came from the co-pol SAR imagery applying the wind direction estimation algorithm described in Section 4.0 above.

GMF	Bias [m]	Standard Deviation [m]	Correlation
Co pol GMF	1.94	4.85	0.70
HV GMF	0.11	3.75	0.83
HV GMF wind direction dependent	-0.69	3.79	0.85
VH GMF	-1.48	3.22	0.8

Table 3: Statistical results of comparison from SAR retrieved wind speeds to SFMR retrieved wind speeds.

7. Comparing scattering trends to models

Figure 7 indicates that the data shows trends in cross-pol NRCS with respect to wind direction that have not all been reported previously, and which appears to decrease with increasing wind speed. As discussed above, these trends are important to consider when building the inverse functions for estimating wind speed from the cross-pol NRCS values. In addition, Figure 7 indicates that there is little to no trend with incidence angle.

It is of interest to see if these trends can be reproduced from simple scattering models for cross-pol data, and thus generate some sense of what may be generating them. Two scattering mechanism are considered; a tilted ocean surface facet that is rough due to the small scale waves (where the tilting comes from the slopes of the long-scale waves that the facet is riding on), and a breaking water region which is a facet riding on the front slope of a dominant wave and is a rough surface caused by the breaking water. For the tilted ocean surface scattering a standard two-scale model with Bragg Scattering (or Small Perturbation Method) is utilized (Romeiser et al., 1997, Wackerman et al., 2002) and for the breaking water region a Kirchoff Approximation is used to handle the rougher surfaces (Leader, 1971; Fung et al. 1992). Thus the final model for NRCS is

$$\sigma_o = (1 - b_r) \int\int \sigma_b(s_u, s_c) \rho(s_u, s_c) ds_u ds_c + b_r \sigma_{br}, \tag{3}$$

where b_r is the fraction of the surface that is breaking and thus determines the component of the total NRCS that comes from breaking water surfaces (the second term in Eq. (3)) versus the component that comes from the tilted ocean surface (the first term in Eq.(3)).

The first term in Eq. (3) is the standard two-scale model where s_u is the upwind slope of the facet and s_c the crosswind slope respectively. These slopes come from the long-scale waves that are tilting the facet as they pass through. The term $\sigma_b(s_u, s_c)$ is the tilted Bragg NRCS for a facet with slopes s_u and s_c, where the scattering is coming from the roughness of the facet caused by the small-scale waves within the facet (Valenzuela, 1978; Romeiser et al., 1997). The final term $\rho(s_u, s_c)$ is the probability density function for the slopes.

For the breaking water NRCS in Eq. (3), σ_{br}, Bragg scattering is used with the modifications that the G_V and G_H terms are approximations to the Kirchoff Approximation scattering equations (instead of from the Small Perturbation Method) and the surface spectrum Ψ comes from laser measurements of breaking water regions (Walker et al., 1996; Ericson et al., 1999) modified so as to reproduce like-polarization X-band NRCS observations (Walker et al., 1996; Ericson et al., 1999, Haller and Lyzenga, 2003).

The strength of the cross-polarization NRCS in this model will be proportional to a coefficient C that is a function of the rotation of the facet in the range and azimuth directions. This is true for both the two-scale model term as well as the breaking water NRCS term. Using the notation in (Valenzuela, 1978, Eq. 5.3) this coefficient, C, can be written as:

$$C = \frac{\sin^2(\theta_O + \phi_R)\cos^2(\phi_A)\cos^2(\phi_A)}{1 - \cos^2(\theta_O + \phi_R)\cos^2(\phi_A)} \tag{4}$$

where ϕ_R is the rotation of the facet in the radar range direction and ϕ_A is the rotation of the facet in the radar azimuth direction. For a cross-polarization NRCS to exist, the facet must have some rotation in azimuth, with the peak NRCS occurring around 30° to 50° of azimuth rotation. It is this azimuth rotation of the surface that de-polarizes the return and thus generates a cross-polarization NRCS.

We used a JONSWAP wind wave spectrum (Hasselmann et al., 1973) with a *cos(ϕ_w/2)**(2n)* angular dependency where *n*=8 with wind speeds of 10, 15, 20 m/s, incidence angles from 20 to 60° every 5°, and look directions from 0 to 180° every 10°. The wind speed dependence from the Monahan and O'Muircheartaigh (1980) equation was used for whitecap coverage versus wind speed as the breaking fraction value, b_r, modified by a large constant (1.5e-5) to account for the fact that what a radar sees as breaking water is often steepened short-scale waves that extend over larger spatial extents than whitecap coverage.

The model results are shown in Figure 12. The left column plots total NRCS as a function of look direction for each of the three wind speeds. The range of points at each look direction comes from various incidence angles.The right column plots NRCS values that are within ±10° of upwind or downwind (blue diamonds) and ±10° of crosswind (red squares) as a function of incidence angle. Figure 12 only plots look angles from 0° to 180° degrees since the model would generate the same values for 0 to -180° degrees. Figures 7 and 12 show similar trends, a strong look angle dependence at lower wind speed that starts to disappear at higher winds and a relatively constant incidence angle dependence. Note that only the first half of the look angle results in Figure 7 are reproduced in Figure 12.

Clearly, this analysis cannot be considered a model validation. If the breaking water response is decreased by 3 dB and/or the breaking fraction is changed then the breaking water NRCS term would not have been large enough to flatten out the look angle dependency at 20 m/s wind. If a less severe angular distribution had been used for the wind wave spectrum, e.g. *n*=4 instead of *n*=8, then the upwind/crosswind ratio of the model NRCS in Figure 12 would have been much closer to one and not as similar to the data trends in Figure 7. Thus there is enough uncertainty in the model inputs to generate NRCS model results that can vary from a good comparison to the data to no comparison at all. Significantly more data observations would be needed to be able to determine the range of model inputs required to reproduce the data trends over all observations. However, the purpose here was to determine if a reasonable scattering model could reproduce the observed trends as a function of look angle and incidence angle. By comparing Figures 12 and 7 it appears that they can be reproduced by combining scattering from breaking water regions and tilted ocean surfaces using standard models, and that it may be important to consider these trends in building the inverse codes for estimating wind speed.

Finally, we determined whether cross-talk between the channels could be used to explain the observed trends without the need for other scattering models. The specification for Radarsat-2 indicates that the isolation is better than -32 dB between V and H. All of the modeling discussed above can also be used for like-polarization (the Bragg scattering model in Eq. (4) will change) so a VV term can easily be added into the output multiplied by -32 dB to model the isolation. For this test we set the cross-polarization return to a constant value so as to have

no trends in look angle or incidence angle. This does generate a trend with look angle strictly from the cross-talk contamination, but it does not change as significantly with wind speed as is observed in the data. In addition, the resulting incidence angle trend is more severe than observed in the data. That it does not appear that cross-talk contamination by itself is sufficient to explain the observed trends.
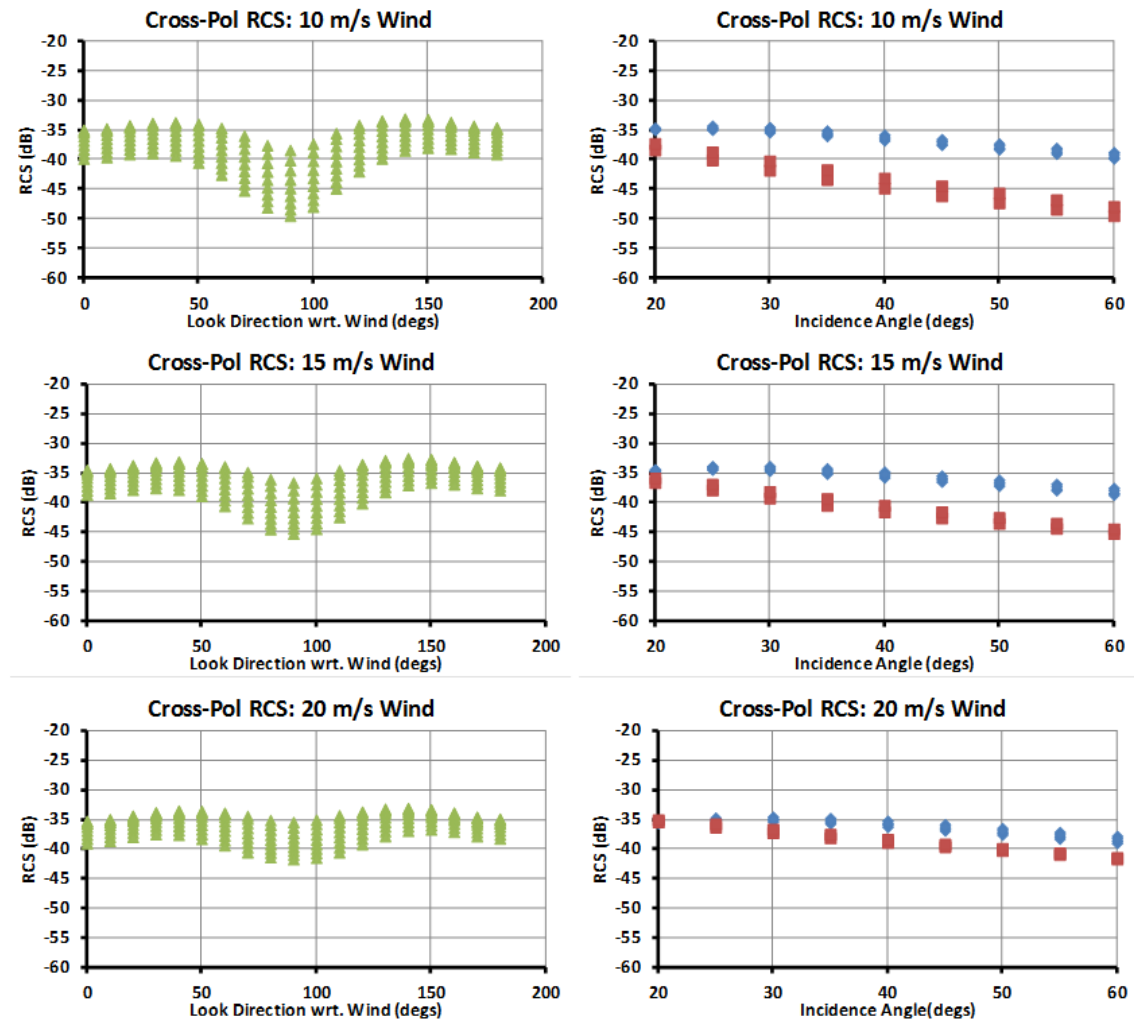

Figure 12: Model results for 3 wind speeds (top plots 10 m/s, middle plots 15 m/s, bottom plots 20 m/s) showing trends with respect to look direction (left column) and incidence angle (right column). For incidence angle, the blue diamonds are within ±10 degrees of either upwind or downwind and the red squares are within ±10 degrees of crosswind. Comparing these plots with the data trends in the observations in Figure 7 shows similar trends: a look angle dependence that flattens out at higher wind speeds and very little variation in incidence angle.

8. Conclusion and Outlook

Previous work has shown that there is some utility in using cross-polarized SAR images in estimating wind speeds, particularly under high wind speed conditions. In this paper we investigate this utility further using a set of simultaneous co-polarized and cross-polarized SAR images collected over typhoons with coincident in situ measurements of wind speed from an airborne SFMR sensor as well as wind speed and directions observations from

dropsondes deployed by the aircraft. Our conclusions based on this data set are summarized as follows.

1. We believe that it is important to remove the noise effects and sensor artifacts before analyzing the cross-polarized radar cross section (RCS) values versus surface winds. Thus in this study we removed scalloping, beam seams, nadir ambiquities, and most importantly the sensor noise floor, before analyzing the RCS values.
2. Contrary to previous work, we observe a dependence of cross-polarized RCS with wind direction (with respect to the SAR look direction) in addition to wind speed. This dependence can be re-produced using simple scattering models and thus may be due to a combination of tilted Bragg scattering and scattering from breaking water regions. It does not appear to be due to cross-talk effects. We also observe a slight trend with incidence angle, that can also be reproduced using simple scattering models, but it is small enough that we do not consider it in the GMF analysis.
3. Using this data we have derived new GMFs that convert cross-polarized SAR RCS into wind speed both with and without the wind direction dependence. Uses the wind direction dependent GMF gives improved wind speed estimations than not including this dependency, but note that this means we need simultaneous co-polarized SAR imagery to derive the wind direction (since we can not derive it independently from only the cross-polarized SAR image). All of the cross-polarized GMFs (i.e. with or without wind direction dependence) provide significantly improved wind speed estimation of the co-polarized SAR images when compared to in situ wind speed measurements taken within the typhoon. This appears to confirm the hypothesis that the cross-polarized RCS does not suffer from high wind speed saturation effects that are evident in the co-polarized RCS values. However, this analysis was limited to wind speeds greater than 10 m/s. Due to its proximity to the sensor noise floor, cross-polarized SAR images can not reliably estimate wind speeds that are less than 10 m/s, whereas co-polarized SAR images have been shown to work well from 5 – 20 m/s which indicates that they can also work well in typhoons up to 35 m/s (Horstmann et al., 2013).

Based on this analysis, it appears that the best estimates of wind speed will come from simultaneous co-polarized and cross-polarized SAR imagery. The co-polarized imagery can provide wind direction estimates to use in the cross-polarized GMF. The co-polarized image can also provide improved wind speed estimates for the lower wind speed regions (less than 10 m/s). The cross-polarized image can provide significantly improved wind speed estimates for the higher wind speed regions (greater than 20 m/s), with the two images providing estimates in the middle range (10 – 20 m/s) that can be averaged to decrease noise in the wind speed estimates

Refferences

E.A. Ericson, D.R. Lyzenga, D.T. Walker, 1999, Radar Backscatter from Station Breaking Waves, *J. Geophy. Res.,* **104**, 29679-29695.
A.K. Fung, Z. Li, K.S. Chen, 1992, Backscattering from a Randomly Rough Dielectric Surface, *IEEE Trans. Geosc. Remote Sens.,* **30,** 356-369.

P.W. Gaiser, K.M. St. Germain, E.M.Twarog, G.A. Poe, W. Purdy, D. Richardson, W. Grossman, W.L. Jones, D. Spencer, G. Golba, J. Cleveland, L, Choy, R.M. Bevilacqua, and P. Chang, 2004, The WindSat Spaceborne Polarimetric Microwave Radiometer: Sensor Description and Early Orbit Performance, *IEEE Trans. Geosci. Remote Sensing*, **42**(11), 2347-2360, 2004.

T. Gerling, 1986, Structure of the Surface Wind Field from Seasat SAR, *J. Geophys. Res.,* **91**, 2308–2320.

M. Haller and D.R. Lyzenga, 2003, Comparison of Radar and Video Observations of Shallow Water Breaking Waves*, IEEE Trans. Geosc. Remote Sens.,* **41**, 832-844.

K. Hasselmann, T.P. Barnett, E. Bouws, H. Carlson, D.E. Cartwright, K. Enke, J.A. Ewing, H. Gienapp, D.E. Hasselmann, P. Kruseman, A. Meerburg, P. Müller, D.J. Olbers, K. Richter, W. Sell, and H. Walden, 1973, Measurements of Wind-Wave Growth and Swell Decay during the Joint North Sea Wave Project (JONSWAP)," *Ergänzungsheft zur Deutschen Hydrographischen Zeitschrift Reihe* A(8) (Nr. 12), **95**.

H. Hersbach, A. Stoffelen, and S. de Haan, 2007, An Improved C-band Scatterometer Ocean Geophysical Model Function: CMOD5, *J. Geophys. Res.*, vol. 112, no. C3, p. C03 006.

H. Hersbach, 2010, Comparison of C-Band Scatterometer CMOD5.N Equivalent Neutral Winds with ECMWF. *J. Atmos. Oceanic Technol.*, **27**, 721–736, doi: http://dx.doi.org/10.1175/2009JTECHO698.1

J. Horstmann, W. Koch, S. Lehner, and R. Tonboe, 2000, Wind Retrieval over the Ocean Using Synthetic Aperture Radar with C-band HH Polarization, *IEEE Trans. Geosci. Remote Sens.*, **38**(5), 2122–2131.

J. Horstmann, W. Koch, S. Lehner, and R. Tonboe, 2002, Ocean winds from RADARSAT-1 ScanSAR, *Can. J. Remote Sens.*, **28**(3), 524-533.

J. Horstmann , D. R. Thompson, F. Monaldo, S. Iris, and H. C. Graber, 2005, Can Synthetic Aperture Radars be used to Estimate Hurricane Force Winds? *Geophys. Res. Lett.,* **32,** L22801, doi:10.1029/2005GL023992.

J. Horstmann, and W. Koch, 2005, Comparison of SAR Wind Field Retrieval Algorithms to a Numerical Model Utilizing ENVISAT ASAR Data, *IEEE Journal of Oceanic Engineering*, **30**(3), 508-515, doi 10.1109/JOE.2005.857514.

J. Horstmann, C. Wackerman, S. Falchetti, and S. Maresca, 2013, Tropical Cyclone Winds Retrieved from Synthetic Aperture Radar, *Oceanography*, **26**(2), 46–57, DOI:10.5670/oceanog.2013.30, 2013.

P.A. Hwang, B. Zhang, and W. Perrie, 2010, Depolarized Radar Return for Breaking Wave Measurements and Hurricane Wind Retrieval. *Geophys. Res. Lett.,* **37,** L01604, doi:10.1029/2009GL041780.

K.B. Katsaros, P.W. Vachon, P.G. Black, P.P. Dodge and E.W. Uhlhorn, 2000, Wind Fields from SAR: Could they Improve our Understanding of Storm Dynamics? *Johns Hopkins APL Technical Digest,* **21,** 86–93.

K.B. Katsaros, P. W. Vachon, W. T. Liu, and P. G. Black, 2002, Microwave Remote Sensing of Tropical Cyclones from Space. *J. Oceanogr.,* **58,** 137–151.

W. Koch, 2004, Directional Analysis of SAR Images Aiming at Wind Direction, *IEEE Trans. Geosci. Remote Sensing*, DOI 10.1109/TGRS.2003.818811, **42**, 702-710.

S. Lehner, J. Horstmann, W. Koch, and W. Rosenthal, 1998, Mesoscale Wind Measurements using Recalibrated ERS SAR Images, *J. Geophys. Res.,* **103**(C4), 7847–7856.

J.C. Leader, 1971, The Relationship between the Kirchoff Approach and Small Perturbation Analysis in Rough Surface Scattering, *IEEE Trans. Ant. Prop.,* **19**, 786-788.

E.C. Monahan, I. O'Muircheartaigh, 1980, Optimal Power Law Description of Oceanic Whitecap Coverage Dependence on Wind Speed, *J. Phys. Oceanogr.*, **10**, 2094-2099.

F. M. Monaldo, D. R. Thompson, W. G. Pichel, and P. Clemente-Colon, 2004, A systematic comparison of QuikSCAT and SAR ocean surface wind speeds, *IEEE Trans. Geosci. Remote Sens.,* **42**(2), 283–291.

A. Mouche, D. Hauser, J.-F. Daloze, and C. Guerin, 2005, Dual Polarization Measurements at C-band Over the Ocean: Results from Airborne Radar Observations and Comparison with ENVISAT ASAR Data, *IEEE Trans. Geosci. Remote Sens*., **43**(4), 753–769.

A. Reppucci, S. Lehner, J. Schulz-Stellenfleth, and S. Brusch, 2010, Tropical Cyclone Intensity Estimated from Wide-swath SAR Images. *IEEE Trans. Geosci. Remote Sens.,* **48,** 1639–1649.

R. Romeiser, J. Horstmann, M.J. Caruso, and H.C. Graber, 2012, A Descalloping Post-Processor for ScanSAR Images of Ocean Scenes, *IEEE Trans. Geosci. Remote Sens.,* **51**(6), 3259-3272, DOI 10.1109/TGRS.2012.2222648.

R. Romeiser, W. Alpers, V. Wismann, 1997, An Improved Composite Surface Model for the Radar Backscattering Cross Section of the Ocean Surface: 1. Theory of the Model and Optimization/Validation by Scattering Data, *J. Geophy. Res.,* **102**, 25237-25250.

H. Shen, W. Perrie, and Y. He, 2009, A New Hurricane Wind Retrieval Algorithm for SAR Images, *Geophys. Res. Lett.,* **33**, L21812, doi:10.1029/2006GL027087.

H. Shen, Y. He, and W. Perrie, 2009, Speed Ambiguity in Hurricane Wind Retrieval from SAR Imagery, *Int. J. Remote Sens.,* **30**, 2827–2836.

D. Thompson, T. Elfouhaily, and B. Chapron, 1998, Polarization Ratio for Microwave Backscattering from the Ocean Surface at Low to Moderate Incidence Angles, 1998, *in Proc. Int. Geosci. Remote Sens. Symp. 1998*, Seattle, USA.

R. Touzi, P. W. Vachon, and J. Wolfe, 2010, Requirement on Antenna Cross-Polarization Isolation for the Operational use of C-band SAR Constellations in Maritime Surveillance, *IEEE Geosci. Remote Sens. Lett.,* **7**, 861–865.

E.W. Uhlhorn, P. G. Black, J. L. Franklin, M. Goodberlet, J. Carswell, and A. S. Goldstein, 2007, Hurricane Surface Wind Measurements from an Operational Stepped Frequency Microwave Radiometer, *Mon. Wea. Rev*., **135**, 3070–3085.

P. Vachon and F. Dobson, 2000, Wind Retrieval from RADARSAT SAR Images: Selection of a Suitable C-band HH Polarization Wind Retrieval Model, *Can. J. Remote Sens.*, **26**(4), 306–313.

P. Vachon and J. Wolfe, 2011, C-band Cross-polarization Wind Speed Retrieval, *IEEE Geosci. Remote Sens. Lett.,* **8,** 456–459.

G.R. Valenzuela, 1978, Theories for the Interaction of Electromagnetic and Oceanic Waves – A Review, *Boundary-Layer Meteor*., **13**, 61-85, 1978.

J. Verspeek, A. Stoffelen, M. Portabella, H. Bonekamp, C. Anderson, and J. Figa Saldaña, 2010, Validation and calibration of ASCAT using CMOD5.n, *IEEE Trans. Geosci. Remote Sens.*, **48**(1), 386–395.

C. Wackerman, C. Rufenach, R. Schuchman, J. Johannessen, and K. Davidson, 1996, Wind Vector Retrieval using ERS-1 Synthetic Aperture Radar Imagery, *J. Geophys. Res.*, **34**, 1343–1352.

C. Wackerman, P. Clemente-Colon, W.G. Pichel, X. Li, 2002, A Two-scale Model to Predict C-band VV and HH Normalized Radar Cross Section Values over the Ocean, *Can. J. Remote Sens*., **28**, 367-384.

D.T. Walker, D.R. Lyzenga, E.A. Ericson, D.E. Lund, 1996, Radar Backscatter and Surface Roughness Measurements for Stationary Breaking Waves*, in Proc. R. Soc. Lond. A*, **452**, 1953-1984.

G.-J. van Zadelhoff, A Stoffelen, P. W. Vachon, J. Wolfe, J. Horstmann, and M. Belmonte Rivas, 2013, Scatterometer Hurricane Wind Speed Retrievals using Cross Polarization, *Atmos. Meas. Tech. Discuss*., **6**, 7945-7984, doi:10.5194/amtd-6-7945-2013.

B. Zhang, W. Perrie, and Y. He, 2011, Wind Speed Retrieval from RADARSAT-2 Quad-polarization Images using a New Polarization Ratio Model. *J. Geophys. Res.,* **116,** C08008, doi:10.1029/2010JC006522.

B. Zhang and W. Perrie, Cross-Polarized Synthetic Aperture Radar- A New Potential Measurements Technique for Hurricanes*, Bull. Amer. Meteor. Soc.,* **93**, 531–541, doi: http://dx.doi.org/10.1175/BAMS-D-11-00001.1